How Centrifugal Breakout from Magnetic B-stars Controls the Onset of Their Hα Emission

S. Owocki[1,2], M. E. Shultz[1], A. ud-Doula[3] and J. Sundqvist[4]

1. Department of Physics & Astronomy, University of Delaware, Newark, DE 19716 USA
2. Bartol Research Insitute, University of Delaware, Newark, DE 19716 USA
3. Penn State Scranton, 120 Ridge View Dr., Dunmore, PA 18512, USA
4. KU Leuven, Instituut voor Sterrenkunde, Celestijnenlaan 200D, 3001 Leuven, Belgium

Strongly magnetic B-type stars with moderately rapid rotation form 'centrifugal magnetospheres' (CMs), from the magnetic trapping of stellar wind material in a region above the Kepler co-rotation radius. A longstanding question is whether the eventual loss of such trapped material occurs from gradual drift/diffusive leakage, or through sporadic '*centrifugal break out*' (CBO) events, wherein magnetic tension can no longer contain the built-up mass. We argue here that recent empirical results for Balmer-α emission from such B-star CMs strongly favor the CBO mechanism. Most notably, the fact that the onset of such emission is largely *independent* of the stellar luminosity strongly disfavors any drift/diffusion process, for which the net mass balance would depend on the luminosity-dependent wind feeding rate. In contrast, we show that in a CBO model the equilibrium mass in the magnetosphere is indeed independent of this wind feeding rate, and has a dependence on field strength and Kepler radius that naturally explains the empirical scalings for the onset of Hα emission. However, the general lack of observed Balmer emission in late-B and A-type stars could still be attributed to a residual level of diffusive or drift leakage that does not allow their much weaker winds to fill their CMs to the breakout level needed for such emission.

1 Introduction

In the subset ($\sim$10%) of massive stars with strong ($>$ 100G), globally ordered (often primarly dipolar) magnetic fields, the trapping of stellar wind outflow by closed magnetic loops leads to the formation of a circumstellar *magnetosphere* (Petit et al., 2013). Because of the rotational spindown associated with their relatively strong, magnetized wind (ud-Doula et al., 2009), magnetic O-type stars are typically slow rotators, with trapped wind material falling back on a dynamical timescale, giving what's known as a "dynamical magnetosphere" (DM). But in magnetic B-type stars, the relatively weak stellar winds imply longer spin-down times, and so a significant fraction that still retain a moderately rapid rotation; in cases that the associated Keplerian corotation radius $R_{\rm K}$ lies within the Alfvén radius $R_{\rm A}$ that characterizes the maximum height of closed loops, the rotational support leads to formation of a "*centrifugal magnetosphere*" (CM), wherein the trapped wind material accumulates into a relatively dense, stable and long-lived 'rigidly rotating magnetosphere' (RRM) (Townsend & Owocki, 2005, hereafter TO05).

A key question has been what loss process(es) eventually balance the steady feeding of the CM by the stellar wind. The appendices of TO05 presented an analytic

analysis of the 'centrifugal break out' (CBO) expected to occur (e.g., Havnes & Goertz, 1984) when the mass build-up leads to a centrifugal force that overwhelms the magnetic tension confining disk material. This CBO narrative has been challenged by Townsend et al. (2013), who argued that the overall CM mass inferred from circumstellar photometric absorption is substantially below (by a factor ∼50) the breakout scalings from TO05. But through a more extensive and MHD-calibrated analysis of CBO, we find much lower CM masses, which in fact are now quite compatible with such empirical estimates. We further show (see figure 2) that the CBO model provides a good explanation for the sudden onset of Balmer emission at a critical value of the Kepler radius magnetic field, as well as its *independence* of the luminosity-dependent wind-mass-loss-rate.

2 Centrifugal Breakout Scalings

2.1 Disk surface density and optical depth

Following the appendices of TO05, we ground our analysis of CM mass distribution and its associated Balmer emission on the simple aligned-dipole case, for which the angle between the rotational and magnetic axes $\beta = 0$. In this case, the CM accumulation surface is a simple disk in the common equatorial plane for both the magnetic field and stellar rotation, with centrifugal support maintained for all radii r at or above the Kepler co-rotation radius, $R_{\rm K}$ ($\equiv (GM/\Omega^2)^{1/3}$, for stellar mass M and rotation frequency Ω, with gravitation constant G).

Equation (A4) of TO05 gives an expression for a characteristic surface density σ_* for CBO. Applying the symbol definitions given there, this can readily be translated into an expression for surface density as a function of the field strength B_K and gravity $g_{\rm K} = GM/R_{\rm K}^2$ at the Kepler radius $R_{\rm K}$,

$$\sigma_* = \frac{B_{\rm K}^2}{4\pi g_{\rm K}}\,. \tag{1}$$

Multiplying both sides by the gravity $g_{\rm K}$, and noting that the magnetic term is related to the magnetic pressure $P_{\rm B} = B_{\rm K}^2/8\pi$, we see that this has a similar scaling to that for hydrostatic equilibrium, wherein the pressure at any level is just given by gravity times the column mass of material above, $P = \sigma g$.

The high radiation temperature of B-stars means that any circumstellar Hydrogen in their CMs should be nearly fully ionized, with any observed Balmer-α emission arising from recombination cascades that include transition from level 3 to 2. Since the associated recombination rate depends on the product of the number densities of protons and electrons, which scales with the square of the mass density as $n_{\rm e} n_{\rm p} \sim \rho^2$, the associated emissivity likewise scales as $\eta \sim \rho^2$. In terms of an associated absorption opacity κ and absorptivity $\kappa\rho$, we can then define a source function $S \equiv \eta/(\kappa\rho)$, which for an LTE process like recombination is generally set by the temperature-dependent Planck function. Assuming the disk temperature T at any radius r does not vary much with height z above the disk, the wavelength dependent specific intensity (a.k.a. surface brightness) I_λ from the disk is then given by the formal solution for the radiative transfer,

$$I_\lambda(r,\mu) = S(r)\left[1 - e^{-\tau_\lambda(r)/\mu}\right]\,, \tag{2}$$

where $\tau_\lambda(r)$ is the line optical depth at wavelength λ through the disk normal at radius r, while μ is the projection cosine of the line-of-sight to the disk normal.

Within the TO05 RRM model, the volume density at any given radius r has a gaussian stratification from its midplane value $\rho_m(r)$,

$$\rho(z,r) = \rho_{\rm m}(r) e^{-(z/h)^2} \,, \tag{3}$$

where h is a characteristic scale height. Writing the line-center opacity as $\kappa_{\rm o} = C_{\rm o}\rho$, where $C_{\rm o}$ is a coefficient derived from the specific radiative transfer model, the optical depth is given by integration of $\kappa_{\rm o}\rho = C_{\rm o}\rho^2$ over the full height range $(-\infty < z < \infty)$ through the disk. Using the fact that $\sigma = \rho_{\rm m} h\sqrt{\pi}$, we find the associated line-center optical depth near the Kepler radius scales as

$$\tau_* = \frac{C_{\rm o}\sigma_*^2}{\sqrt{2}\,\pi h_{\rm K}} = \frac{C_{\rm o}}{16\sqrt{2}\pi^3 h_{\rm K}}\,\frac{B_{\rm K}^4}{g_{\rm K}^2} = \frac{C_{\rm o}}{32\pi^3 c_{\rm s}}\,\frac{B_{\rm K}^4 R_{\rm K}^{5/2}}{(GM)^{3/2}} \,. \tag{4}$$

Here the second equality uses equation (1) and the fact that the disk scale height $h_{\rm K}$ at the Kepler radius depends on the sound speed $c_{\rm s}$ and stellar rotation frequency $\Omega \equiv 2\pi/P$:

$$h_{\rm K} = \frac{\sqrt{2}c_s}{\Omega} \,, \tag{5}$$

and the final equality uses the fact that $\Omega = \sqrt{g_{\rm K}/R_{\rm K}}$.

A key result from equation (4) is that this disk optical depth near the Kepler radius depends very sensitively on the field strength length there, scaling as $\tau_* \sim B_{\rm K}^4$. Because in the RRM model the disk surface density has its maximum value near the Kepler radius, its optical depth likewise is greatest there, and so first crosses from optically thin to thick when $\tau_* = 1$. For an optically thin disk with $\tau_* < 1$, expansion of the formal solution (2) shows that the normal ($\mu = 1$) surface brightness scales as $I_1(R_{\rm K}) = S(R_{\rm K})\tau_*$, which is a factor $\tau_* \ll 1$ less than the saturated brightness $I_1(R_{\rm K}) = S(R_{\rm K})$ in the optically thick limit $\tau_* \gg 1$. Since $\tau_* \sim B_{\rm K}^4$, this helps explain the sudden onset of detectable emission at a critical value of $B_{\rm K}$, as shown in the rightmost panel figure 3 from Shultz et al. (2020).

2.2 Calibration by MHD simulations

Following the TO05 development of the RRM model for CMs, ud-Doula et al. (2008) carried out full 2D numerical MHD simulations of magnetically confined stellar winds for the axisymmetric case of aligned-dipole stellar rotation. For cases with sufficiently strong field confinement and rapid rotation (*i.e.*, with Kepler radius well within the Alfven radius, $R_{\rm K} \ll R_{\rm K}$), results showed the overall time-averaged, equilibrium mass in the resulting CM agrees quite well with the predicted analytic scalings for CBO given by TO05 equation (A11).

To facilitate computation here of Balmer emission from such CMs, we have now derived associated results for the time-averaged surface density from these same 2D MHD simluations. Figure 7 of ud-Doula et al. (2008) plots the disk mass distribution $\mathrm{d}m/\mathrm{d}r$ vs. radius and time, for a mosaic of models with various rotation parameters $W \equiv V_{\rm rot}/V_{\rm orb}$ and magnetic confinement parameters, $\eta_* \equiv B_*^2 R_*^2/\dot{M}v_\infty$, with the solid and dashed horizontal lines showing the associated Alfven radii $R_{\rm A} \sim \eta_*^{1/4}$ and Kepler radii $R_{\rm K} \sim W^{-2/3}$.

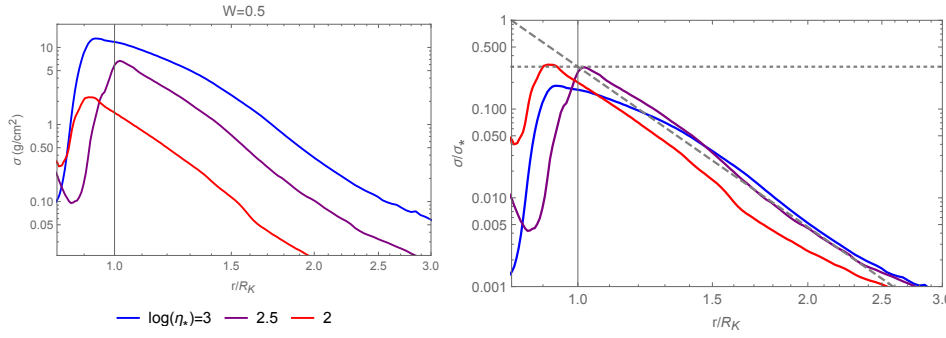

Fig. 1: *Left:* Disk surface density averaged over the last 1.5 Msec for the 2D-MHD simulations from ud-Doula et al. (2008), plotted vs. radius over Kepler radius, $r/R_{\rm K}$, for a model series with ratio of equatorial rotation speed to surface orbital speed, $W \equiv V_{\rm rot}/V_{\rm orb} = 0.5$, giving a Kepler corotation radius to stellar radius of $R_{\rm K}/R_* = W^{-2/3} = 1.6$. The legend marks the colors for the various assumed values of the magnetic confinement parameter η_*. *Right:* For these same 3 cases, the radial variation of MHD surface density normalized by the analytic Kepler radius values in equation (1). The thin vertical line shows that the intermediate confinement model (purple curve) has a peak very near the Kepler radius, but the horizontal dotted line shows that the peak value is a factor 0.3 lower than the analytic predication for σ_*. The diagonal dashed line shows the radial decline from the Kepler radius closely follows a power law, $(r/R_{\rm K})^{-q}$, with $q \approx 6$.

For the case with moderately rapid rotation, $W = 1/2$ ($R_{\rm K} = 1.59R_*$), the left panel of figure 1 here now shows the associated time-averaged (over the final 1500 ks of the simulations) surface density $\sigma = ({\rm d}m/{\rm d}r)/(2\pi r)$, plotted on a log-log scale vs. the radius scaled by the Kepler radius, $r/R_{\rm K}$. The legend shows the line style for each values of $\log \eta_*$. Note that for these strong confinement cases[1] in the simulations, $\log \eta_* = 2$, 2.5 and 3, the surface density peaks near the Kepler radius, then shows nearly a linear decline outward on this log-log scale, indicating a power law.

For these 3 strongest confinement models, the right panel of figure 1 rescales these surface densities by the analytic breakout value from equation (1), σ/σ_*. The horizontal dotted line at a value of 0.3 shows that the peak density at the Kepler radius is actually reduced by about 30% from the analytic value given in equation (1). The slanting dashed line shows a power-law decline from this Kepler value, $\sigma/\sigma_* = 0.3(r/R_{\rm K})^{-q}$, with slope[2] $q = 6$. The fit to the intermediate confinement case $\log \eta_* = 2.5$ is quite good. For $\log \eta_* = 2$ and 3, the peaks occur somewhat below $r = R_{\rm K}$, but even for these cases, the radial declines closely parallel the dashed line.

For the emission model computations in this paper, we thus adopt an MHD-

[1] Because of numerical issues stemming from field-line stiffness and the associated increase in the Alfven speed, the MHD simulations by ud-Doula et al. (2008) were limited to cases with confinement parameters $\eta_* \leq 1000$, much less than the $\eta_* \sim 10^6$ inferred for B-star CMs showing H-α emission. None the less, these simulations had strong-enough confinement to illustrate the CBO process and calibrate its associated scaling relations.

[2] This is significantly steeper than the $q = 3$ index generally assumed for the RRM model, based on an assumption of a fixed time for wind feeding at a rate $\dot{\sigma} \sim B(r) \sim 1/r^3$.

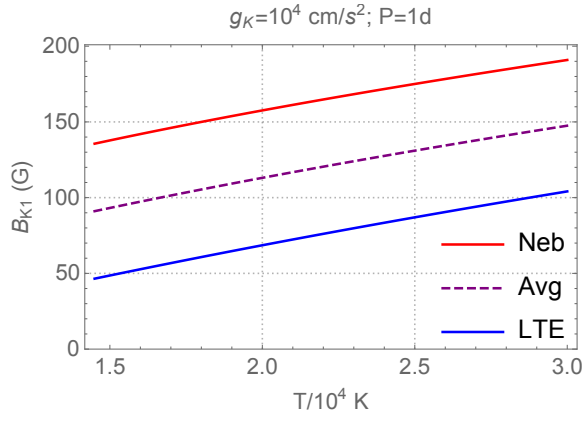

Fig. 2: For a star with rotation period $P = 1$ day and Kepler radius gravity $g_{\rm K} = 10^4$ cm s^{-2}, the critical field $B_{\rm K1}$ vs. disk temperature T for both the nebular (red curve) and LTE (blue curve) models for Hα formation. The black dashed curve shows the average between the two models. Equation (9) gives a simple analytic scaling formula for $B_{\rm K1}$.

calibrated scaling for the surface density given by

$$\sigma(r) = 0.3\,\sigma_* \left(\frac{r}{R_{\rm K}}\right)^{-6} . \tag{6}$$

With this scaling, we can generalize equation (4) to obtain the radial variation of line-center optical depth,

$$\tau_{\rm o}(r) = \frac{C_{\rm o}\sigma^2(r)}{\sqrt{2}\pi h(r)} = 0.09\tau_* \left(\frac{r}{R_{\rm K}}\right)^{-12} \frac{h_{\rm K}}{h(r)} , \tag{7}$$

where the scale height variation $h_{\rm K}/h(r) = \sqrt{3-2(R_{\rm K}/r)^3}$ (Townsend & Owocki, 2005) ranges from unity at $R_{\rm K}$ to a factor $\sqrt{3}$ at large radii. Apart from this modest radial increase, the optical depth drops very steeply with radius, as $\tau_{\rm o} \sim r^{-12}$, leading to quite sharp outer edges to disk emission.

2.3 Critical field evaluation

With this MHD calibration for disk density and thus optical depth, let us next determine the critical field strength $B_{\rm K1}$ for making the disk become optically thick. From (7), we the have $\tau_{\rm K} \equiv \tau_{\rm o}(R_{\rm K}) = 0.09\tau_* \sim B_{\rm K}^4$, so the critical field condition $\tau_{\rm K} = 1$ solves to

$$B_{\rm K1} = \left(\frac{16\sqrt{2}\,\pi^3 h_{\rm K}}{0.09\,C_{\rm o}}\right)^{1/4} \sqrt{g_{\rm K}} \tag{8}$$

$$\approx (70{\rm G}\,T_{\rm 20kK} + \Delta B)\,\sqrt{g_{\rm K4}}\,P_{\rm day}^{1/4} . \tag{9}$$

The latter equality gives an analytic fit form, with $T_{\rm 20kK} \equiv T/20{\rm kK}$, $g_{\rm K4} \equiv g_{\rm K}/(10^4\,{\rm cm\ s^{-2}})$, $P_{\rm day}$ the rotation period in days, and ΔB an optional offset for using a nebular vs. LTE model for Hα opacity.

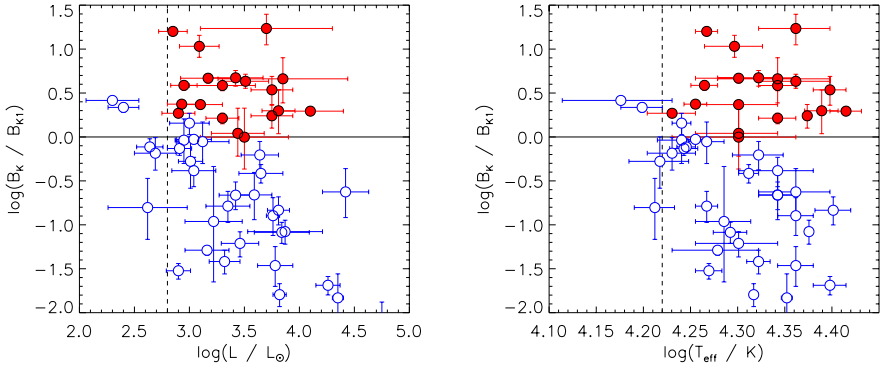

Fig. 3: *Left*: Observed magnetic B-stars plotted in the $\log B_K/B_{K1}$ vs. $\log L/L_\odot$ plane, with stars showing Hα emission in filled red circles, and those without emission in open blue circles. *Right*: Same as top, but plotted vs. log of stellar effective temperature (in K).

For $P_{\rm day} = g_{K4} = 1$, figure 2 compares the variation of B_{K1} vs. disk temperature T for the nebular (red) vs. LTE (blue) models for the Balmer-line opacity; note they both have a roughly linear increase with temperature, with the nebular value showing a nearly fixed offset $\Delta B_{\rm neb} \approx +90$ G.

Indeed, the average between the LTE and nebular models (shown by the dashed line in figure 2) can be approximated simply by setting $\Delta B = \Delta B_{\rm neb}/2 = 45$ G in equation (9). This average gives typical critical fields $B_{K1} \approx 100$ G, in remarkably good agreement with the empirically inferred value for onset for Hα emission, as shown by Shultz et al. (2020). Overall then, choosing ΔB =0, 45, or 90 G represents respectively the LTE, average, or nebular models for opacity.

3 Comparison with Observations

As noted in the introduction, a key motivation for the theoretical analysis in this paper was the result – shown in Shultz et al. (2020) – that the *onset* of detectable Hα occurs at critical value of the Kepler radius field strength, $B_K \approx 100$ G.

Choosing the *average* between the nebular and LTE opacities, and assuming a constant disk temperature $T_K \approx T_{\rm eff}$, we thus apply the inferred values for rotation period P and Kepler gravity g_K to derive for each star in our sample values for B_{K1}, and associated values for the ratio $b_K \equiv B_K/B_{K1}$. Figure 3 here then plots the stars in the $\log b_K$ vs. $\log L$ (top panel) and $\log b_K$ vs. $\log T_{\rm eff}$ (bottom panel) planes, marking those with detectable emission with filled red circles, and those without with open blue circles. Note that the horizontal line at $B_K = B_{K1}$ does remarkably well at separating the stars with and without detectable emission, as well as or better than the empirical separations in Shultz et al. (2020).

This represents strong evidence that centrifugal breakout is the mechanism controlling the mass loss from the CMs in these early to mid-B type magnetic stars.

Note, however, that to the left of the *vertical* dashed lines at $\log(L/L_\odot) = 2.8$ and $\log(T_{\rm eff}/{\rm K}) = 4.22$ ($T_{\rm eff} = 16.6$ kK, corresponding to spectral type B6), even

stars *above* the horizontal line for $B_K = B_{K1}$ show *no* detectable emission. This is likely associated with the sharp drop in radiatively driven stellar wind mass loss rates for such lower luminosity stars. It suggests that there may be other competing mechanism for mass leakage from these CMs, perhaps associated with the drift and diffusion processes discussed by Owocki & Cranmer (2018).

Alternatively, the mass loss for these stars is near the value expected for the onset of *ion runaway* (see eq. 23 of Owocki & Puls, 2002). This occurs when the wind density becomes so low that heavy minor ions that line-scatter stellar radiation are no longer well coupled by Coulomb collisions to the protons. Since the resulting *metal ion wind* thus lacks the hydrogen central to Hα emission, a transition to ion runaway could be the key to the observed lack of emission for stars with lower luminosity and effective temperature than the critical values marked by the vertical dashed lines in figure 3.

To summarize, this transition to no emission in magnetic stars with $\log L/\mathrm{L}_\odot < 2.8$ (or $\log T_{\rm eff}/\mathrm{K} < 4.22$) could either provide a diagnostic for residual leakage by drift or diffusion, or alternatively for an ion runaway transition to a metal ion wind without the Hydrogen needed for Hα emission, or perhaps both.

4 Discussion

The total mass in the CM can be computed from integrating outward from the Kepler radius,

$$\begin{aligned} M_{\rm CM} &\equiv \int_{R_K}^{\infty} \sigma(r)\, 2\pi r\, dr = 0.6\pi\sigma_* \int_{R_K}^{\infty} \left(\frac{r}{R_K}\right)^{-6} r\, dr \\ &= 0.6\frac{B_K^2 R_K^2}{16 g_K} = 0.0375 \frac{B_*^2 R_*^4}{g_* R_K^2}\,. \end{aligned} \tag{10}$$

By comparison, equation (A11) of Townsend & Owocki (2005) derived a similar expression for the asymptotic disk mass m_∞, which has the same parameter scaling, but which is about a factor 8 ($\approx \sqrt{\pi}/6/0.0375$) higher than the expression (10) for the total CM mass derived here. Moreover, in their example application of this scaling for the parameters inferred for the prototypical CM star σ Ori E, Townsend & Owocki (2005) quote a total mass $m_\infty = 9.4 \times 10^{-8}\,\mathrm{M}_\odot$. But in deriving this value, they erroneously applied the inferred *polar* value for the surface field, $B_{\rm p} \approx 10^4$ G, whereas the magnetic confinement in their breakout analysis is set by the field strength at the magnetic *equator*, $B_* = B_{\rm p}/2$. Since $m_\infty \sim B_*^2$, this makes their quoted value a further factor 4 too high.

This is significant because a key critique against the CBO scenario later raised by Townsend et al. (2013) was that the CM mass they inferred from photometric absorption by CM clouds was much less than the putative values inferred from the breakout analysis in Appendix A of Townsend & Owocki (2005). Specifically, for their assumed parameters for σ Ori E, – viz. $M_\star = 8.3\,\mathrm{M}_\odot$, $R_* = 3.77\,\mathrm{R}_\odot$, $R_K = 2.54 R_*$, $B_{\rm p} = 11,000$ G – they inferred an asymptotic breakout mass $m_\infty \approx 1.2 \times 10^{-8}\,\mathrm{M}_\odot$, nearly two orders of magnitude higher than their empirically estimated upper limit, $2 \times 10^{-10}\,\mathrm{M}_\odot$. By comparison, if we apply these same parameters in our equation (10), we obtain for the total CM mass $M_{\rm CM} \approx 3.8 \times 10^{-10}\,\mathrm{M}_\odot$, which is now within a factor two of their empirically inferred value.

The upshot here is that the basic scaling for surface density in our MHD-calibrated breakout analysis, grounded by equation (1) (which is based on equation (A4) from Townsend & Owocki (2005)), is in fact quite compatible with empirical inferences based on photometric absorption, as well as the observed level of polarization (Carciofi et al., 2013).

5 Summary

Let us conclude with an itemized summary of the analysis and results of this paper.

- Motivated by the empirical discovery by Shultz et al. (2020) that the onset of detectable Hα emission from centrifugal magnetospheres (CMs) in magnetic B-stars is *independent* of stellar luminosity, and thus of the stellar wind feeding rate of the CM, we have reexamined (Townsend & Owocki, 2005) here the notion that the eventual loss of CM mass occurs through *centrifugal breakout* (CBO).

- Our CBO analysis predicts a quantitative scaling for the level and radial distribution of CM surface density $\sigma(r)$ (equations (1) and (6)). The associated optical depth in Hα scales with Kepler radius values $\tau_{\rm K} \sim \sigma(R_{\rm K})^2 \sim B_{\rm K}^4$, with thus a sudden onset of detectable emission at a critical Kepler field $B_{\rm K1}$ (equation (8)) that gives $\tau_{\rm K} = 1$, as demonstrated by figure 3.

- While the CBO model explains well the emission onset in early- to mid-B stars, spectral types later than about B6 (with $T_{\rm eff} \lesssim 16\,{\rm kK}$ and luminosity $L \lesssim 800\,{\rm L}_\odot$) show *no* emission, even for stars with $B_{\rm K} > B_{\rm K1}$. This might signify a residual diffusive/drift leakage that prevents the lower stellar wind mass loss from filling the CM to the level needed for Hα emission, or alternatively might result from a transition to a metal-ion wind that lacks the requisite Hydrogen. Or perhaps a combination of both.

- The total CM mass from the MHD-calibrated CBO analysis here is an order of magnitude lower than previous estimates, and is no longer incompatible with values inferred empirically by Townsend et al. (2013). This and the quasi-steady nature of breakout in 3D models thus effectively mitigate these authors' arguments against the CBO paradigm.

A forthcoming follow up to this study (Owocki et al., 2020) shows that the line-profile shapes and emission line equivalent widths predicted by this CBO model also agree well with observations for these same sample of magnetic B-stars marked in figure 3 as showing Hα emission.

References

Carciofi, A. C., Faes, D. M., Townsend, R. H. D., Bjorkman, J. E., *ApJ* **766**, 1, L9 (2013)

Havnes, O., Goertz, C. K., *A&A* **138**, 421 (1984)

Owocki, S. P., Cranmer, S. R., *MNRAS* **474**, 3, 3090 (2018)

Owocki, S. P., Puls, J., *ApJ* **568**, 965 (2002)

Owocki, S. P., Shultz, M. E., ud-Doula, A., Sundqvist, J. O., *MNRAS* (2020)

Petit, V., et al., *MNRAS* **429**, 398 (2013)
Shultz, M. E., et al., *MNRAS* (2020)
Townsend, R. H. D., Owocki, S. P., *MNRAS* **357**, 251 (2005)
Townsend, R. H. D., et al., *ApJ* **769**, 1, 33 (2013)
ud-Doula, A., Owocki, S. P., Townsend, R. H. D., *MNRAS* **385**, 97 (2008)
ud-Doula, A., Owocki, S. P., Townsend, R. H. D., *MNRAS* **392**, 1022 (2009)

Left: Stan Owocki. Right: John Landstreet.

Asif ud-Doula.